

# The relation between atomic gas and star formation rate densities in faint irregular galaxies

Sambit Roychowdhury,<sup>1\*</sup> Jayaram N. Chengalur,<sup>2\*</sup> Serafim S. Kaisin<sup>3\*</sup>  
and Igor D. Karachentsev<sup>3\*</sup>

<sup>1</sup>Max-Planck-Institut für Astrophysik, Karl-Schwarzschild-Str. 1, 85748 Garching, Germany

<sup>2</sup>NCRA-TIFR, Post Bag 3, Ganeshkhind, Pune 411 007, India

<sup>3</sup>Special Astrophysical Observatory, Russian Academy of Sciences, N. Arkhyz, KChR 369167, Russia

## ABSTRACT

We use data for faint ( $M_B > -14.5$ ) dwarf irregular galaxies drawn from the FIGGS survey to study the correlation between the atomic gas density ( $\Sigma_{\text{gas,atomic}}$ ) and star formation rate ( $\Sigma_{\text{SFR}}$ ) in the galaxies. The estimated gas phase metallicity of our sample galaxies is  $Z \sim 0.1 Z_\odot$ . Understanding star formation in such molecule poor gas is of particular importance since it is likely to be of direct relevance to simulations of early galaxy formation. For about 20% (9/43) of our sample galaxies, we find that the HI distribution is significantly disturbed, with little correspondence between the optical and HI distributions. We exclude these galaxies from the comparison. We also exclude galaxies with very low star formation rates, for which stochastic effects make it difficult to estimate the true star formation rates. For the remaining galaxies we compute the  $\Sigma_{\text{gas,atomic}}$  and  $\Sigma_{\text{SFR}}$  averaged over the entire star forming disk of the galaxy. For these galaxies we find a nearly linear relation between the star formation rate and the atomic gas surface densities, viz.  $\log \Sigma_{\text{SFR}} = 0.91^{+0.23}_{-0.25} \log \Sigma_{\text{gas,atomic}} - 3.84^{+0.15}_{-0.19}$ . The corresponding gas consumption timescale is  $\sim 10$  Gyr, i.e. significantly smaller than the  $\sim 100$  Gyr estimated for the outer regions of spiral galaxies. We also estimate the gas consumption timescale computed using the global gas content and the global star formation rate for all galaxies with a reliable measurement of the star formation rate, regardless of whether the HI distribution is disturbed or not. The mean gas consumption timescale computed using this entire gas reservoir is  $\sim 18$  Gyr, i.e. still significantly smaller than that estimated for the outer parts of spirals. The gas consumption timescale for dwarfs is intermediate between the values of  $\sim 100$  Gyr and  $\sim 2$  Gyr estimated for the outer molecule poor and inner molecule rich regions of spiral disks.

**Key words:** galaxies: dwarf – radio lines: galaxies – ultraviolet: galaxies

## 1 INTRODUCTION

The rate at which gas is converted into stars in galaxies is an important input into understanding galaxy formation and evolution. However, despite decades of studies it remains poorly understood, mainly because, the exact processes that govern this transition are complex (see e.g. McKee & Ostriker 2007) and difficult to capture in their entirety in analytical or numerical models. Most models hence use empirical star formation “recipes” to model the formation of stars (e.g. see Schaye & Dalla Vecchia 2008; Governato et al. 2010; Hopkins et al. 2013; Fu et al. 2013). These recipes are generally based on scaling relations between gas

density and star formation rate that have been established via observations of nearby galaxies. One of the most commonly used parameterizations of this type is the Kennicutt-Schmidt relation (Schmidt 1959; Kennicutt 1998) which relates the surface densities of gas ( $\Sigma_{\text{gas}}$ ) and star formation rate surface density ( $\Sigma_{\text{SFR}}$ ) through a power law. The power law index found by Kennicutt (1998) (i.e.  $N \sim 1.4$ ) was based on a sample of spiral and star bursting galaxies. The variation of this relationship with environment remains an area of active research. There have also been a number of recent studies of the correlation between the molecular gas surface density  $\Sigma_{\text{H}_2}$  and  $\Sigma_{\text{SFR}}$ , but there is still no consensus regarding the values of the parameters of the power law used to characterise this correlation. For e.g. Leroy et al. (2013) find the coefficient of the power law to be  $N \sim 1 \pm 0.15$ , while Momose et al. (2013) find that it could be as steep as  $N \sim 1.8$ . Regarding the correlation between

\* E-mail: sambit@mpa-garching.mpg.de (SR); chengalu@ncra.tifr.res.in (JNC); skai@sao.ru (SSK); ikar@sao.ru (IDK)

the atomic gas surface density  $\Sigma_{\text{gas,atomic}}$  and the  $\Sigma_{\text{SFR}}$  the situation appears still more complex. In the central parts of spiral galaxies, the HI gas density appears to be uncorrelated to  $\Sigma_{\text{SFR}}$  while in the outer, molecule poor regions, the two appear to be significantly correlated (Bigiel et al. 2010). Understanding star formation in molecule poor gas is of particular importance since it is likely to be of direct relevance in cosmological simulations of early galaxy formation.

This paper is part of an ongoing study regarding star formation in molecule poor gas in nearby, very faint dwarf galaxies. Our studies are based on samples drawn from the Faint Irregular Galaxy GMRT Survey (FIGGS Begum et al. 2008). In Roychowdhury et al. (2009) it was shown that  $\Sigma_{\text{gas,atomic}}$  and  $\Sigma_{\text{SFR}}$  are correlated on sub-kpc scales, and that in general the power law index is steeper than the value of 1.4 found by Kennicutt (1998). In Roychowdhury et al. (2011) we showed (again on sub kpc scales) that all regions with  $\Sigma_{\text{gas,atomic}} \gtrsim 10 \text{ M}_{\odot} \text{pc}^{-2}$  have some associated star formation, but that the fraction of gas with associated star formation decreases steadily as  $\Sigma_{\text{gas,atomic}}$  decreases. Since star formation is likely to proceed via the formation of molecular gas, this means that the molecular fraction is significant for all gas with  $\Sigma_{\text{gas,atomic}} \gtrsim 10 \text{ M}_{\odot} \text{pc}^{-2}$ . The number of FIGGS galaxies with FUV and H $\alpha$  observations has increased significantly since the work of Roychowdhury et al. (2011). *Spitzer* observations of dust emission are also available for several of these galaxies, which allows us to correct for dust extinction using the recent “composite” star formation calibrations. In this paper we use the new observational data, and the new calibrations to study the relationship between  $\Sigma_{\text{gas,atomic}}$  and  $\Sigma_{\text{SFR}}$  averaged over the entire star forming disk, as well as computed using the total gas content and the total star formation rate. We also compare our results with those obtained from studies of nearby spiral galaxies. The conditions in ISM in dwarf galaxies is expected to be similar to that of the outskirts of spiral disks, in that both are molecule poor. However, the faint dwarfs that we study here have somewhat lower metallicity (viz.  $Z \sim 0.1 Z_{\odot}$ ) than what is typical in the outskirts of spirals (viz.  $Z \sim 0.4 - 0.6 Z_{\odot}$ ; Carraro et al. 2007; Genovali et al. 2014). Further, as compared to the outskirts of spirals, the gas in our sample galaxies experiences less rotational shear.

## 2 SAMPLE AND METHODOLOGY

The galaxy sample that we use in this paper are summarised in Table 1. The columns in the table are: column (1) the name of the galaxy, columns (2) and (3) the coordinates in the J2000 system, column (4) the absolute B-band magnitude from Begum et al. (2008), column (5) the distance in Mpc, column (6) the B-band diameter at 26.5 magnitude  $\text{arcsecond}^{-2}$  (i.e. the Holmberg diameter), column (7) the measured apparent axial ratio in the B-band. The values for columns (5), (6) and (7) are from Karachentsev et al. (2013). Column (8) gives the estimated gas phase metallicity (see Section 2.1 for details). As mentioned above, the galaxies are drawn from the FIGGS sample – the current subsample includes all galaxies in that sample with available FUV and/or H $\alpha$  data. The FUV data are taken from the public *GALEX* archive. The H $\alpha$  data are either from our observations using the 6m BTA telescope in Russia (Karachentsev & Kaisin 2007; Kaisin & Karachentsev 2008; Karachentsev & Kaisin 2010; Kaisin, Karachentsev & Kaisina 2011), or drawn from the literature if we did not have 6m BTA H $\alpha$  map for a galaxy. In Table 1 column (9) gives the FWHM of the HI beam for each galaxy in

arcseconds. The choice of the beam size to make the neutral hydrogen maps is discussed in the following section. Column (10) gives the resolution of the 6m BTA telescope H $\alpha$  images. *GALEX* FUV images have a resolution of  $\sim 4.5$  arcseconds.

### 2.1 Estimates of the Gas and Star Formation Rate density

The aim of our study is to study the relationship between the surface densities of gas ( $\Sigma_{\text{gas}}$ ) and star formation ( $\Sigma_{\text{SFR}}$ ) for the sample galaxies. These surface densities are measured as the average over the ‘star-forming disk’ of each galaxy, which we define as the Holmberg ellipse. We restrict the calculated values to the ‘star-forming disk’ in order to make a comparison between the current star formation and gas present in the region where star formation is occurring. The assumption is hence that the remaining gas is not involved in the current star formation. We relax this assumption in Sec. 3.4 and compute the relation between the total gas content and the total star formation rate. Figure A1 shows overlays of the HI, FUV and H $\alpha$  emission along with the Holmberg ellipse for galaxies in the sample. As can be seen, the H $\alpha$  emission is generally centrally concentrated and overlaps with the regions with the highest HI column density. For most galaxies, the FUV emission is also restricted to within the Holmberg ellipse. This provides further justification for assuming that the gas within the Holmberg ellipse is most related to the ongoing star formation. For a handful of galaxies some very low level FUV emission lies outside the Holmberg ellipse. For these galaxies we increase the size of the axes for the ‘star-forming disk’ by 10%, (consistent with the estimate of maximum error on the Holmberg ellipse parameter measurements). The resultant ellipse now contains all the FUV emission. These galaxies are marked in Table 2 and in the overlays (see online version).

Total intensity HI maps were used to determine the average column density within the ‘star-forming disk’. In keeping with our previous work (Roychowdhury et al. 2009, 2011) we made HI column density maps of all our sample galaxies at the uniform sub-kpc linear resolution of  $\sim 400$  pc. This was the best achievable resolution while ensuring that significant amount of extended low level emission is not missed due to the decreasing signal-to-noise with increasing resolution for all of our sample galaxies. The FWHM of our HI column density maps (listed in Table 1) are comparable to those used for many previous works studying disk-averaged Schmidt type relations including Kennicutt (1998); Wyder et al. (2009). The atomic gas density is corrected for the presence of helium by multiplying by a factor of 1.34. No correction is made for the presence of molecular gas (but see the discussion in Sec. 4). The face on surface densities are computed by correcting for the inclination of the disks, assuming that they are oblate spheroids (a valid assumption considering the luminosity range of the dwarf irregular galaxies in our sample, e.g. see Roychowdhury et al. 2013). We multiply the measured surface density by the cosine of the inclination angle in order to estimate the face on column density. The details of how the *GALEX* FUV and BTA H $\alpha$  observations are converted to fluxes are given in Roychowdhury et al. (2009, 2011). Briefly, foreground stars and background galaxies in the FUV and H $\alpha$  images are masked. When calculating  $\Sigma_{\text{SFR}}$ , the flux of either tracer is averaged over the non-masked area for that tracer. For fluxes taken from the literature, surface densities are obtained by dividing by the area of the Holmberg ellipse (corrected for inclination). The observed H $\alpha$  fluxes have to be corrected for contamination from NII, before they can be used for SFR estimation. For the low metallicity dwarfs in our sample, this correction is generally negligible. For three of our sample galaxies for which we have H $\alpha$

**Table 1.** Sample parameters

Galaxy	$\alpha$ (J2000) ( <sup>h</sup> <sup>m</sup> <sup>s</sup> )	$\delta$ (J2000) ( <sup>°</sup> <sup>'</sup> <sup>''</sup> )	$M_B$	D (Mpc)	$D_{H\alpha}$ ( <sup>'</sup> )	b/a	$Z/Z_\odot$	HI beam " × "	H $\alpha$ resolution "
And IV	00 42 32.30	+40 34 19	−8.39	6.3	1.00	0.77	0.06	13.9×12.7	
DDO 226	00 43 03.80	−22 15 01	−14.17	4.9	2.24	0.36	0.12	16.8×16.8	
DDO 6	00 49 49.30	−21 00 58	−12.5	3.34	2.29	0.41	0.07	26.5×20.6	
UGC 685	01 07 22.44	+16 41 04	−14.31	4.5	2.40	0.71	0.20*	16.8×16.0	1.9
KK 14	01 44 42.80	+27 17 19	−12.13	7.2	0.79	0.37	0.06	13.4×10.0	1.4
KK 41	04 25 20.00	+72 48 30	−14.06	3.9	3.72	0.57	0.11	25.8×17.1	2.0
UGCA 92	04 32 04.90	+63 36 49	−15.65	3.01	2.00	0.50	0.19	30.2×24.2	
KKH 34	05 59 40.40	+73 25 40	−12.30	4.6	0.93	0.56	0.06	20.0×16.0	
UGC 5186	07 13 51.60	+10 31 19	−14.90	6.96	1.86	0.59	0.15	11.8×11.1	1.5
DDO 43	07 28 17.20	+40 46 13	−14.75	7.8	1.41	0.69	0.14	11.7×09.5	
KK 65	07 42 31.98	+16 33 40	−14.29	7.62	1.12	0.56	0.12	11.5×10.3	2.1
UGC 4115	07 57 01.80	+14 23 27	−14.27	7.5	1.91	0.56	0.12	11.0×11.0	
KDG 52	08 23 56.00	+71 01 46	−11.49	3.55	1.26	0.92	0.05	24.2×21.5	
UGC 4459	08 34 07.20	+66 10 54	−13.37	3.56	2.00	0.87	0.13*	24.9×21.1	1.5
UGC 5186	09 42 58.66	+33 15 56	−12.98	6.9	1.38	0.23	0.08	12.1×10.5	1.9
UGC 5209	09 45 04.20	+32 14 18	−13.15	6.7	0.83	0.96	0.08	12.8×10.7	
UGC 5456	10 07 19.70	+10 21 44	−15.08	5.6	1.62	0.50	0.16	14.7×14.7	
UGC 6145	11 05 35.00	−01 51 49	−13.14	7.4	1.38	0.56	0.08	11.1×11.1	
UGC 6456	11 27 59.90	+78 59 39	−14.03	4.3	1.48	0.53	0.10†	19.4×17.0	2.5
UGC 6541	11 33 29.10	+49 14 17	−13.71	3.9	1.74	0.57	0.13*	22.7×21.4	
NGC 3741	11 36 06.40	+45 17 07	−13.13	3.0	1.48	0.55	0.09*	28.2×27.0	
DDO 99	11 50 53.00	+38 52 50	−13.52	2.6	4.27	0.37	0.10	31.7×31.7	
E321−014	12 13 49.60	−38 13 53	−12.70	3.2	1.41	0.43	0.07	29.9×21.6	
UGC 7242	12 14 07.40	+66 05 32	−14.06	5.4	1.23	0.42	0.11	15.3×15.3	
CGCG 269−049	12 15 46.63	+52 23 14	−13.25	4.9	1.05	0.30	0.05*	16.8×16.8	2.0
UGC 7298	12 16 30.10	+52 13 39	−12.27	4.21	0.85	0.55	0.06	19.6×19.6	
KK 144	12 25 29.15	+28 28 57	−12.59	6.3	1.12	0.44	0.07	16.0×10.3	1.6
DDO 125	12 27 40.90	+43 29 44	−14.16	2.5	3.89	0.56	0.12	34.8×30.0	2.0
UGC 7605	12 28 38.75	+35 43 03	−13.53	4.43	1.48	0.73	0.10	22.3×14.8	2.0
GR8	12 58 40.40	+14 13 03	−12.11	2.1	1.66	0.91	0.09*	39.3×39.3	
UGC 8215	13 08 03.60	+46 49 41	−12.26	4.5	0.85	0.70	0.06	19.2×17.9	
DDO 167	13 13 22.80	+46 19 11	−12.70	4.2	1.10	0.55	0.07	20.7×18.8	
KK 200	13 24 36.00	−30 58 20	−11.96	4.6	1.10	0.62	0.06	17.9×17.9	
E444−78	13 36 30.80	−29 14 11	−13.3	5.25	1.58	0.42	0.09	15.7×15.7	
UGC 8638	13 39 19.40	+24 46 32	−13.68	4.27	1.66	0.67	0.10	19.3×19.3	2.0
DDO 181	13 39 53.82	+40 44 21	−13.03	3.1	2.40	0.57	0.14*	29.8×25.2	1.4
DDO 183	13 50 51.10	+38 01 16	−13.17	3.24	2.40	0.32	0.09	27.4×24.5	
UGC 8833	13 54 48.70	+35 50 15	−12.42	3.2	1.17	0.89	0.07	26.4×25.2	
KK 230	14 07 10.70	+35 03 37	−9.55	1.9	0.76	0.83	0.03	43.4×43.4	
DDO 187	14 15 56.50	+23 03 19	−12.51	2.5	1.70	0.76	0.11*	33.0×33.0	
KK 246	20 03 57.40	−31 40 54	−13.69	7.83	0.91	0.42	0.10	10.5×10.5	
UGCA 438	23 26 27.50	−32 23 26	−12.94	2.2	2.14	0.80	0.08	37.5×37.5	
KKH 98	23 45 34.02	+38 43 04	−10.78	2.5	1.05	0.55	0.04	34.5×31.6	2.7

\*: Based on Marble et al. (2010),

†: based on Moustakas &amp; Kennicutt (2006).

observations, the NII flux is available separately. As expected the corrections are small ( $\sim 0.01$  dex in  $\Sigma_{\text{SFR}}$ ). We hence use the NII flux corrected data whenever possible (some literature H $\alpha$  values are already corrected for NII flux contamination, as indicated in Table 2) and ignore the correction otherwise.

The luminosities measured for each sample galaxy is listed in Table 2, FUV in column (2) and H $\alpha$  in column (3). The sources for additional data taken from the literature are also given in Table 2. Columns (4), (5) and (6) provide the references from where values of H $\alpha$  flux, NII flux and 24  $\mu\text{m}$  flux were obtained.

The calibration we use for converting FUV luminosity to SFR

is taken from Kennicutt & Evans II (2012); Hao et al. (2011):

$$\log \frac{\text{SFR}}{M_\odot \text{ yr}^{-1}} = \log \frac{\nu}{\text{Hz}} \frac{L_\nu}{\text{ergs s}^{-1} \text{ Hz}^{-1}} - 43.35 \quad (1)$$

The calibration for converting H $\alpha$  luminosity to SFR is also taken from Kennicutt & Evans II (2012); Hao et al. (2011):

$$\log \frac{\text{SFR}}{M_\odot \text{ yr}^{-1}} = \log \frac{L_{\text{H}\alpha}}{\text{ergs s}^{-1}} - 41.27 \quad (2)$$

These updated calibrations use a Kroupa IMF with mass limits of 0.1 and 100  $M_\odot$ , with a slope of  $-2.35$  between 1 and 100  $M_\odot$  and a slope of  $-1.3$  between 0.1 and 1  $M_\odot$ . The calibrations use the latest Starburst99 codes of Leitherer et al. (1999), but are appropriate for solar metallicity. Our sample galaxies have estimated

**Table 2.** Measured fluxes and literature sources

Galaxy	$L_{FUV}$ (ergs s <sup>-1</sup> Hz <sup>-1</sup> )	$L_{H\alpha}$ (ergs s <sup>-1</sup> )	Reference H $\alpha$ flux	Reference NII flux	Reference 24 $\mu$ m flux
And IV <sup>U d</sup>	$1.0 \times 10^{25}$		1		
DDO 226 <sup>U</sup>	$2.1 \times 10^{25}$		2*		
DDO 6 <sup>m</sup>	$8.3 \times 10^{24}$		3		
UGC 685 <sup>U</sup>	$2.9 \times 10^{25}$	$6.4 \times 10^{38}$		4	5
KK 14 <sup>m</sup>	$7.1 \times 10^{24}$	$3.7 \times 10^{37}$			
KK 41 <sup>m</sup>	$1.5 \times 10^{25}$	$5.4 \times 10^{37}$			
UGCA 92			4*		
KKH 34			1		
UGC 3755 <sup>U</sup>	$1.1 \times 10^{26}$	$1.4 \times 10^{39}$			
DDO 43 <sup>m</sup>	$7.2 \times 10^{25}$		1		
KK 65 <sup>U</sup>	$2.6 \times 10^{25}$	$7.3 \times 10^{38}$			
UGC 4115 <sup>U d</sup>	$1.3 \times 10^{26}$		1		
KDG 52 <sup>m</sup>	$5.7 \times 10^{24}$				5
UGC 4459 <sup>U</sup>	$3.5 \times 10^{25}$	$1.0 \times 10^{39}$		4	5
UGC 5186 <sup>U</sup>	$8.9 \times 10^{24}$	$2.4 \times 10^{36}$			
UGC 5209 <sup>U</sup>	$1.1 \times 10^{25}$		1		
UGC 5456 <sup>U</sup>	$1.2 \times 10^{26}$		1		5
UGC 6145 <sup>U</sup>	$1.3 \times 10^{25}$				
UGC 6456 <sup>U</sup>	$7.9 \times 10^{25}$	$2.0 \times 10^{39}$		4	6
UGC 6541 <sup>m</sup>	$4.6 \times 10^{25}$		4*		5
NGC 3741 <sup>U d</sup>	$2.9 \times 10^{25}$		4*		5
DDO 99 <sup>m</sup>	$2.6 \times 10^{25}$		1		5
E321-014 <sup>m</sup>	$7.0 \times 10^{24}$		3		5
UGC 7242 <sup>U d</sup>	$3.7 \times 10^{25}$				5
CGCG 269-049 <sup>U d</sup>	$1.6 \times 10^{25}$	$1.5 \times 10^{38}$			
UGC 7298 <sup>U d</sup>	$7.4 \times 10^{24}$				
KK 144 <sup>U d</sup>	$1.1 \times 10^{25}$	$5.4 \times 10^{37}$			
DDO 125 <sup>U</sup>	$2.6 \times 10^{25}$	$2.6 \times 10^{38}$			5
UGC 7605 <sup>U</sup>	$3.7 \times 10^{25}$	$2.5 \times 10^{38}$			5
GR8 <sup>U</sup>	$1.5 \times 10^{25}$		1		5
UGC 8215 <sup>U</sup>	$6.0 \times 10^{24}$		1		
DDO 167 <sup>U d</sup>	$1.6 \times 10^{25}$		1		
KK 200 <sup>U</sup>	$4.2 \times 10^{24}$		3		
E444-78 <sup>U</sup>	$1.0 \times 10^{25}$				
UGC 8638 <sup>U</sup>	$3.4 \times 10^{25}$	$2.5 \times 10^{38}$			5
DDO 181 <sup>U d</sup>	$1.9 \times 10^{25}$	$2.5 \times 10^{38}$			5
DDO 183 <sup>U</sup>	$1.6 \times 10^{25}$		1		5
UGC 8833 <sup>U</sup>	$9.1 \times 10^{24}$		1		
KK 230	$6.5 \times 10^{23}$				
DDO 187 <sup>U</sup>	$7.6 \times 10^{24}$		1		
KK 246 <sup>U</sup>	$2.5 \times 10^{25}$				
UGCA 438 <sup>m</sup>	$1.3 \times 10^{25}$		1		
KKH 98 <sup>U d</sup>	$2.4 \times 10^{24}$	$3.0 \times 10^{37}$			

<sup>U</sup>: Galaxies with ‘trustworthy’ SFR<sub>FUV</sub> values (see Section 3.1)

<sup>d</sup>: fluxes summed over ellipse with axes increased by 10% compared to the values listed in Table 1

<sup>m</sup>: galaxies with morphologically disturbed HI (see Section 3.2)

\*: corrected for NII flux.

References– 1: Kennicutt et al. (2008); 2: Meurer et al. (2006); 3: Bouchard, Da Costa & Jerjen (2009); 4: Moustakas & Kennicutt (2006); 5: Dale et al. (2009); 6: Engelbracht et al. (2008).

metallicities significantly lower than solar, and the correction for this is discussed below.

We account for the energy from star formation re-radiated at infra-red wavelengths due to dust using *Spitzer* 24  $\mu$ m data and the new ‘composite’ calibrations. For star formation estimated from FUV we use the relation given by Hao et al. (2011), viz.

$$L_{FUV,corr} = L_{FUV,obs} + 3.89 L_{25 \mu m} \quad (3)$$

which is fed into equation 1 to obtain the SFR.

For star formation estimated from the H $\alpha$  flux we use the cor-

rection given by Kennicutt et al. (2009), viz.

$$L_{H\alpha,corr} = L_{H\alpha,obs} + 0.02 L_{25 \mu m} \quad (4)$$

which is fed into equation 2 to obtain the SFR. Due to the low dust content of our sample dwarf galaxies, the correction from dust obscuration in small. This is shown in Figure 1 where we plot the fractional change in SFR (accounted for the correction due to low metallicity discussed next) on accounting for FUV emission reprocessed by dust for sample galaxies with available 24  $\mu$ m data. *Spitzer* 24  $\mu$ m fluxes are available only for some of the galax-

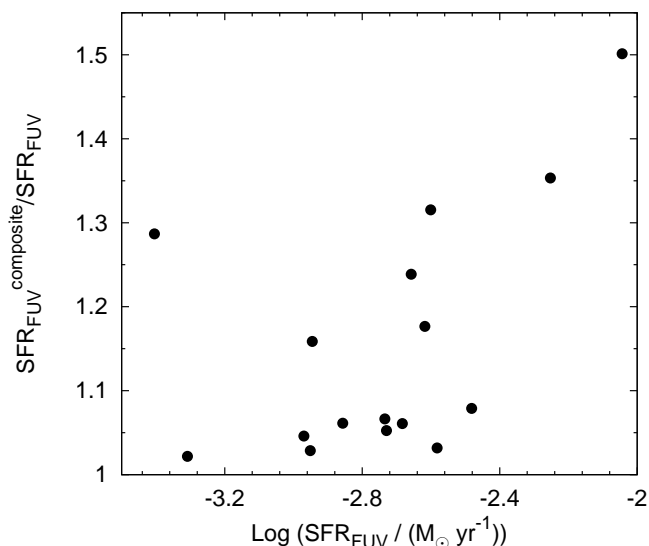


**Figure 1.** For the 16 galaxies with 24  $\mu\text{m}$  data, ratio of the ‘composite’ SFR calculated using eqn. 3 in eqn. 1 to the SFR calculated using eqn. 1 and the FUV flux only, plotted against the latter SFR in log.

ies in our sample. In order to estimate the dust correction for the other galaxies we use the available measurements to estimate how the 24  $\mu\text{m}$  flux varies with the FUV flux. We show in Figures 2 and 3 the 24  $\mu\text{m}$  flux against the SFR, determined without taking into account the IR emission but correcting for metallicity as described in the next paragraph, from FUV and  $\text{H}\alpha$  for galaxies with observed 24  $\mu\text{m}$  fluxes. We fit power laws to both sets of data using the method described in Section 3.3. The plots are shown in Figures 2 and 3 with the corresponding confidence intervals for the best fits, which are given by:

$$\begin{aligned} \log \frac{F_{24\mu\text{m}}}{\text{Jy}} &= 1.78 \log \frac{\text{SFR}_{\text{FUV}}}{\text{M}_{\odot} \text{ yr}^{-1}} + 2.62 \\ \log \frac{F_{24\mu\text{m}}}{\text{Jy}} &= 1.21 \log \frac{\text{SFR}_{\text{H}\alpha}}{\text{M}_{\odot} \text{ yr}^{-1}} + 1.28 \end{aligned} \quad (5)$$

For galaxies without 24  $\mu\text{m}$  data, the expected 24  $\mu\text{m}$  emission is estimated using the above mentioned best fits and the SFR of the galaxy. The estimated dust correction varies from 0.0007 dex to 0.4 dex with a median change of 0.05 dex for  $\Sigma_{\text{SFR}}$  measured using FUV, and varies from 0.006 dex to 0.23 dex with a median change of 0.09 dex for  $\Sigma_{\text{SFR}}$  measured using  $\text{H}\alpha$ . For most of the galaxies in our sample, this estimated correction is hence small.

Finally a correction is necessary in order to account for the low metallicities of our sample galaxies. The oxygen abundance of a handful of our sample galaxies has been measured by Marble et al. (2010). We use the value of solar abundance from Asplund et al. (2009) to arrive at the metallicity for these galaxies, and the resulting values are listed in Table 1. Additionally oxygen and Balmer band line fluxes for UGC 6456 is given in Moustakas & Kennicutt (2006). We use this flux to derive abundance using the method of Pilyugin & Thuan (2005) and hence determine the gas phase metallicity, also listed in Table 1. For the remaining galaxies without measured metallicities, we use the luminosity ( $M_B$ ) – metallicity relation for dIs from Ekta & Chengalur (2010) (the second relation in their Table 4) to estimate their metallicities. Recent es-

timates of emergent fluxes in sub-solar metallicity environments by Raiter, Schaerer & Fosbury (2010) calculated using evolutionary synthesis models using a Salpeter IMF and constant star formation for the last  $10^8$  years show that they increase by  $\sim 11\%$ ,  $19\%$ ,  $27\%$ ,  $32\%$  and  $\sim 18\%$ ,  $38\%$ ,  $67\%$ ,  $85\%$  for FUV and  $\text{H}\alpha$  ionizing fluxes respectively for metallicities of 0.4, 0.2, 0.05, 0.02 times solar. For each sample galaxy we do a linear interpolation between these values and arrive at the percentage increase and hence the correction factor for the emergent flux at the metallicity of that galaxy. Further, in order to account for variations in the IMF and star formation history, we increase the estimated error on these corrected  $\Sigma_{\text{SFR}}$ . Details on this are given in the following section. We use the metallicity corrected  $\Sigma_{\text{SFR}}$  for all further calculations.

### Error estimates

We estimate the error on the measurement of  $\Sigma_{\text{gas,atomic}}$  to be 10%, which accounts for both the noise in the images as well as for errors in the flux calibration. For the  $\Sigma_{\text{SFR}}$  the errors are computed as the quadrature sum of whichever of the following errors are applicable for the galaxy under consideration: flux measurement errors (FUV,  $\text{H}\alpha$ ,  $\text{NII}$ , 24  $\mu\text{m}$ ), 10% flux calibration error for *GALEX* FUV data, 15% flux calibration error for BTA  $\text{H}\alpha$  data. Following Leroy et al. (2012, 2013) an additional 50% error is added in quadrature in order to account for the errors caused by variations in the IMF and star formation history. Whenever SFR was calculated without considering the contribution from 24  $\mu\text{m}$  flux, the error on the calibration was taken to be 30%. For galaxies without measured 24  $\mu\text{m}$  fluxes, the error on the estimated 24  $\mu\text{m}$  fluxes (i.e. those determined using the fits in Eqn. 5) were computed using the 68% confidence intervals shown in Figures 2 and 3. These errors are also added in quadrature to arrive at the total estimated error.

## 3 RESULTS AND DISCUSSION

### 3.1 Comparing the star formation tracers

The tracers that we use here, viz. the  $\text{H}\alpha$  and FUV fluxes, are sensitive to different parts of the stellar IMF.  $\text{H}\alpha$  emission primarily traces massive ( $\gtrsim 16 M_{\odot}$ ) star formation while FUV emission arises from the photospheres of intermediate mass ( $\gtrsim 6 M_{\odot}$ ), longer lived stars. The FUV emission is also more affected by extinction by dust than  $\text{H}\alpha$  emission. These and other phenomena such as the escape of ionizing photons and possible variations in the IMF between galaxies (Weidner & Kroupa 2005; Meurer et al. 2009) can produce differences in the SFRs as estimated using these two different tracers. Such differences are expected to be most pronounced in dwarf irregular galaxies with low overall SFRs. For example, a recent burst of star formation (leading to significant  $\text{H}\alpha$  flux) superposed on a quiescent SFR (which is traced by FUV) can make the SFR estimated using  $\text{H}\alpha$  higher than that traced using FUV. Such mismatches have been observed for several dwarf galaxies (see e.g. Lee et al. 2009b; Hunter, Elmegreen & Ludka 2010), even for some of the galaxies from the present sample (Roychowdhury et al. 2011). A recent work comparing the two SFRs for Local Volume dwarf galaxies which includes all our present sample galaxies observe a similar mismatch at the faint end (Karachentsev & Kaisina 2013). Observations suggest that these differences are unlikely to be due to the escape of ionizing photons (Relaño et al. 2012) or variation in the IMF (Roychowdhury et al. 2011; Weisz et al. 2012;

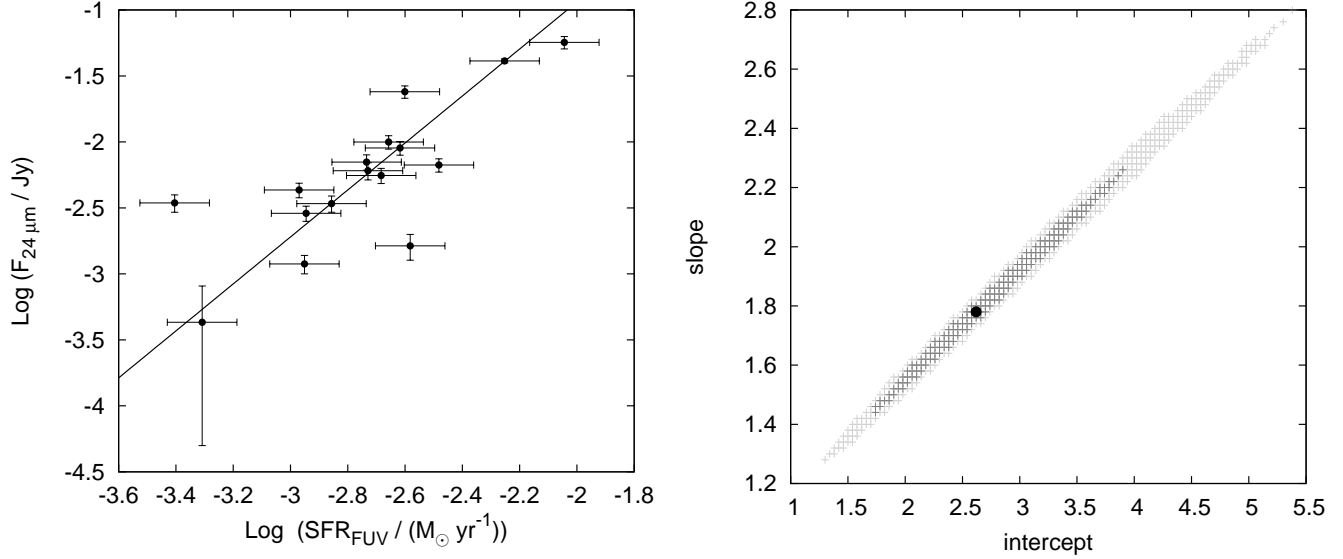


**Figure 2.** Left panel shows the logarithm of measured 24  $\mu\text{m}$  flux plotted against the logarithm of the total star formation rate within the Holmberg ellipse calculated using only FUV flux (and not the ‘composite’ calibration) but after correcting for NII flux (wherever available) and the effect of sub-solar metallicity (see text for details), for sample galaxies with existing 24  $\mu\text{m}$  measurements. The bold line shows the best fit to the points. The right panel shows the best fit (black point) value and 68% (dark grey), 95% (light grey) confidence intervals on the value of slope and intercept.

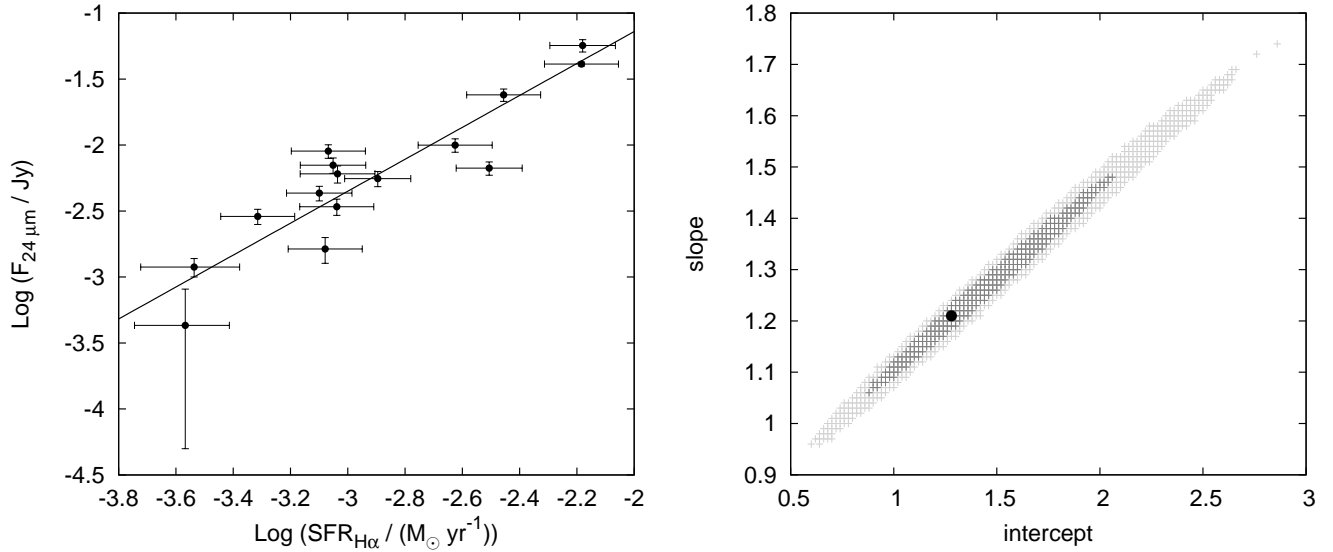


**Figure 3.** Left panel shows the logarithm of measured 24  $\mu\text{m}$  flux plotted against the logarithm of the total star formation rate within the Holmberg ellipse calculated using only H $\alpha$  flux (and not the ‘composite’ calibration) but after correcting for NII flux (wherever available) and the effect of sub-solar metallicity (see text for details), for sample galaxies with existing 24  $\mu\text{m}$  measurements. The bold line shows the best fit to the points. The right panel shows the best fit (black point) value and 68% (dark grey), 95% (light grey) confidence intervals on the value of slope and intercept.

Hermanowicz, Kennicutt & Eldridge 2013). Here we look at the SFRs obtained for our sample galaxies using H $\alpha$  and FUV and see whether the measurements can be reconciled in terms dust attenuation, bursty star formation and stochastic sampling of the IMF.

Figure 4 shows the SFRs calculated using the two different tracers for our sample galaxies plotted against each other. The most noteworthy feature of Fig. 4 is that at low star formation rates (i.e. for  $\log(\text{SFR}/(\text{M}_{\odot} \text{ yr}^{-1})) \lesssim -3.0$ ), the SFR estimated from the

H $\alpha$  flux is systematically smaller than that estimated from the FUV flux. da Silva, Fumagalli & Krumholz (2014) study the stochastic effects at low intrinsic SFRs and how they affect SFR estimates derived using various tracers. They find that as one measures increasingly low SFRs using a particular tracer through a standard calibration function, the posterior probability distribution function (PDF) of the true underlying SFR not only becomes wider (due to the stochastic sampling of the high mass end of the IMF) but

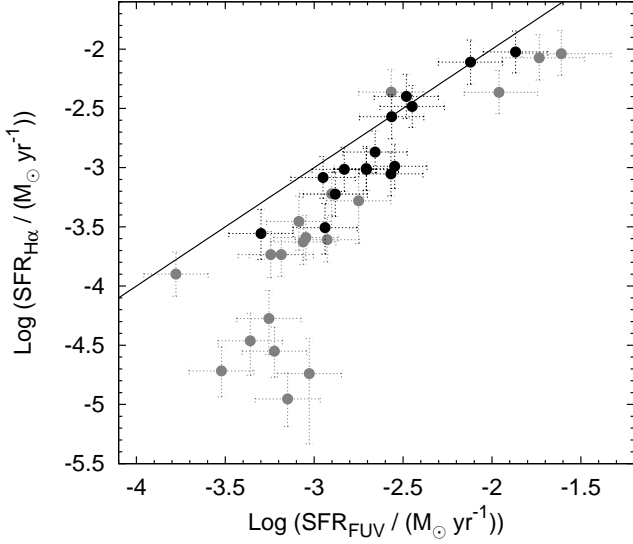


**Figure 4.** Logarithm of total SFRs within the Holmberg ellipse deduced using H $\alpha$  emission and FUV flux plotted against one another. Galaxies with existing 24  $\mu$ m measurements are represented with black circles while the ones without with grey circles. The bold line is the 1:1 line.

also its peak is offset to a higher SFR value than the one measured (due to the increasingly bursty nature of star formation at low SFRs). This is most pronounced when SFR is traced by H $\alpha$  emission. Using the output of their code available online, we study the behaviour of the posterior SFR PDF when varying the SFR as measured using H $\alpha$  or FUV in steps of 0.25 dex. We consider their results for a flat prior distribution of the SFR and with the assumption that all star formation occurs in either clusters or associations, consistent with the increasingly bursty star formation histories with decreasing stellar mass in galaxies (Kauffmann 2014). When using H $\alpha$  as tracer the peak of the posterior PDF is already offset from the measured SFR by more than 0.25 dex for the highest SFRs measured in our sample galaxies, and the offset increases to  $\sim 0.5$  dex for  $\log(\text{SFR}/(\text{M}_\odot \text{yr}^{-1})) \lesssim -2.4$ , and to  $\sim 0.75$  dex for  $\log(\text{SFR}/(\text{M}_\odot \text{yr}^{-1})) \lesssim -3.4$ . The scatter in the posterior SFR PDF is also substantial and increases to more than 1 dex for  $\log(\text{SFR}/(\text{M}_\odot \text{yr}^{-1})) \lesssim -2.5$ . Considering the above facts, we choose  $\log(\text{SFR}/(\text{M}_\odot \text{yr}^{-1})) = -2.5$  as the limiting trustworthy SFR measured using H $\alpha$  emission. When using FUV as a tracer of star formation though, the situation is markedly better. The peak of the posterior SFR PDF shifts by  $\sim 0.25$  dex as compared to the measured SFR only for  $\log(\text{SFR}/(\text{M}_\odot \text{yr}^{-1})) \lesssim -2.8$ , and by  $\sim 0.5$  dex for  $\log(\text{SFR}/(\text{M}_\odot \text{yr}^{-1})) \lesssim -4.9$ . The scatter in the posterior SFR PDF remains low and approaches 1 dex only for  $\log(\text{SFR}/(\text{M}_\odot \text{yr}^{-1})) \lesssim -4$ . Considering the above mentioned values, it becomes obvious that  $\Sigma_{\text{SFR}}$ s obtained for our sample galaxies using FUV as tracer are more trustworthy. We use  $\log(\text{SFR}/(\text{M}_\odot \text{yr}^{-1})) = -4$  as the limiting trustworthy SFR measured using FUV emission.

### 3.2 Morphology of the HI distributions

Having established the regions where the star formation indicators appear to be reliable, we now move on to comparing star for-

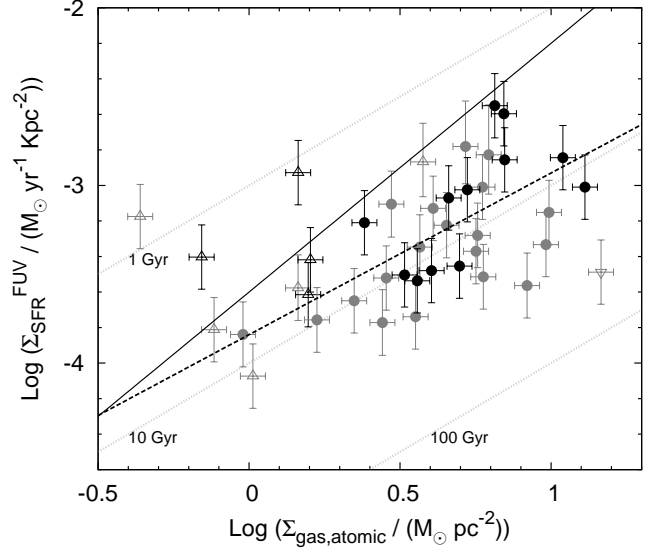


**Figure 5.** Logarithm of disk-averaged surface densities of SFR (deduced using FUV flux) and atomic gas plotted against each other. Black symbols are for galaxies with existing 24  $\mu$ m measurements and grey symbols are for those without. Open upward pointing triangles represent galaxies with disturbed HI morphology whereas open downward pointing triangle represents the only sample galaxy with total SFR below  $-4$  in log. The remaining galaxies are marked with filled circles. The best fit Schmidt law to the remaining galaxies marked with filled circles is shown as the dashed line, whereas the ‘canonical’ Kennicutt-Schmidt law is shown as the bold line. Faint grey dotted lines mark different gas consumption timescales.

mation rate density to the gas surface density. For spiral galaxies, (as detailed in the introduction), these two surface densities are found to be correlated. The situation in very small dwarf galaxies could however be more complex. The shallow potential wells of dwarf galaxies makes it easy for feedback from star formation to have a significant impact on the distribution and kinematics of their gaseous component (e.g. see Mac Low & Ferrara 1999; Governato et al. 2010), but see also Silich & Tenorio-Tagle (2001). In the context of the current study, the principal effect of this feedback is that it could destroy any previously extant correlations between the gas density and the star formation rate. We hence carefully examine all of the HI distributions in our galaxy sample to identify those for which there is a clear signature of the HI gas being disturbed. For 9/43 galaxies (viz. DDO 43, KDG 52, DDO 6, KK 14, KK 41, UGC 6541, DDO 99, E321-014 and UGCA 438) we find that the HI distribution is disturbed. We exclude these 9 galaxies from the analysis below where we compare the gas and star formation surface densities. The “disturbances” vary from the galaxy having an HI “hole” at the center of the disk (e.g. DDO 43 and KDG 52), to galaxies where the HI is misaligned or even non-overlapping with the star forming disk (Figure A1). The fact that about one-fourth of our sample galaxies show *morphological* signatures of disturbed HI distributions is an indication that star formation feedback could be important in dwarf galaxies.

### 3.3 The relation between $\Sigma_{\text{gas}}$ and $\Sigma_{\text{SFR}}$

Figures 5 and 7 show scatter plots of  $\Sigma_{\text{SFR}}$  and  $\Sigma_{\text{gas}}$  for the galaxies in our sample. Galaxies for which the SFR is low enough for

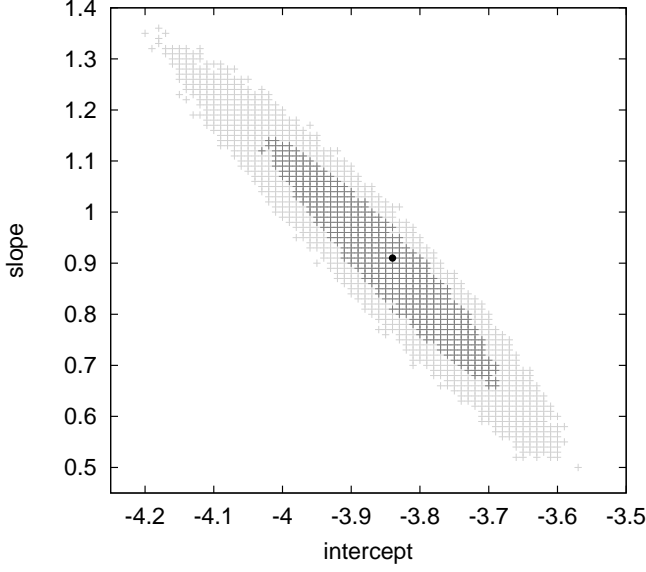


**Figure 6.** Corresponding to the fit shown in Figure 5, the best fit (black point) value and 68% (dark grey), 95% (light grey) confidence intervals on the value of slope and intercept are shown.

stochastic effects to be important (see discussion in Section 3.1) are marked with downward pointing triangles while galaxies with disturbed HI morphology are marked by upward pointing triangles. Two things stand out for these galaxies in line with our expectations, viz. (i) for galaxies with disturbed HI morphology the inferred gas consumption timescales are lower than the average for the sample indicating deficiency (plausibly loss) of HI within the star-forming region. And (ii) for galaxies below the SFR limit for the particular tracer the inferred gas consumption timescales are higher than the average for the sample indicating that the SFR has been underestimated.

In the case of  $\Sigma_{\text{SFR}}^{\text{H}\alpha}$  excluding galaxies with low SFR and/or disturbed HI morphology leaves us with too few (six) galaxies to try and fit a Kennicutt-Schmidt type power law. Nevertheless, it is interesting to note that the gas consumption timescales for these galaxies clusters around  $\sim 10$  Gyr. This is about an order of magnitude shorter than that estimated for the molecule poor outer parts of disk galaxies (Bigiel et al. 2010). For the galaxies with SFR rate estimated from the FUV emission we are left with 31 galaxies after removing galaxies with low SFR and/or disturbed HI. We refer to this sub-sample as the ‘trustworthy’ sub-sample. For these galaxies we determine the best fit linear relation through a Monte-Carlo method which is similar to a direct bivariate linear regression but at the same time provides a way to estimate the error on the fitted quantities notwithstanding the asymmetric error bars in our data.

For each ‘trustworthy’ galaxy, the surface density (HI or SFR) is assumed to have a distribution which is a normalized combination of two Gaussians having mean equal to the actual measurement. Values greater than the actual measurement are drawn from a Gaussian having standard deviation equal to the positive error bar (in real space), whereas values less than the actual measurement are drawn from a Gaussian having standard deviation equal to the negative error bar.  $10^6$  sets of data are simulated, where each set contains one value for each ‘trustworthy’ galaxy drawn randomly from its  $\Sigma_{\text{gas,atomic}}$  and  $\Sigma_{\text{SFR}}$  distributions defined in the above man-

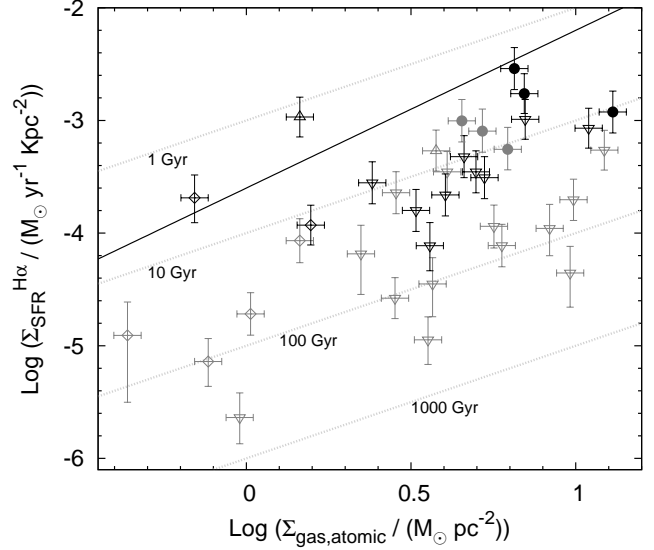


**Figure 7.** Logarithm of disk-averaged surface densities of SFR (deduced using  $\text{H}\alpha$  flux) and atomic gas plotted against each other. Black symbols are for galaxies with existing  $24\ \mu\text{m}$  measurements and grey symbols are for those without. Open upward pointing triangles represent galaxies with disturbed HI morphology, open downward pointing triangles represent galaxies with total SFR lower than the limit below which there would be too few  $\text{H}\alpha$  producing stars whereas open diamonds represent galaxies which have both disturbed HI morphology and total SFR below the ‘trustworthy’ threshold. (see text for details). The remaining galaxies are marked with filled circles. Points with dashed errorbars represent galaxies with literature  $\text{H}\alpha$  data. The ‘canonical’ Kennicutt-Schmidt law is shown as the bold line. Faint grey dotted lines mark different gas consumption timescales.

ner. Straight lines are fitted to each of the  $10^6$  sets of data through bivariate linear regression, with the point for any galaxy weighted by the quadrature mean of the higher and lower error bars. The peak of the  $10^6$  straight line fits (the best fit) is shown as the dashed line in Figure 5, and also as the black point in Figure 6. Figure 6 also shows the 68% and 95% confidence intervals for the values of slope and intercept thus determined as the dark and light grey shaded areas respectively. Using the extent of the 68% confidence interval, the Kennicutt-Schmidt law using only atomic gas for the faint dwarf irregular galaxies in our sample is given as:

$$\log \Sigma_{\text{SFR}} = 0.91^{+0.23}_{-0.25} \log \Sigma_{\text{gas,atomic}} - 3.84^{+0.15}_{-0.19} \quad (6)$$

In order to provide a straightforward comparison with Kennicutt (1998) we also determine the regression relation using the same procedure as followed in that paper. This recovers the same value for the mean slope (0.91) and almost the same value for the mean intercept ( $-3.87$ ) as above.

In Figure 8 we compare the data for our galaxies (i.e. the ‘trustworthy’ sub-sample) with that for other samples. The data on circumnuclear starbursts and spirals are from Kennicutt (1998), and the are the ones based on which the ‘canonical’ Kennicutt-Schmidt law was defined. Values for low surface brightness (LSB) galaxies are from Wyder et al. (2009), who also estimate the gas surface density only using atomic gas. It is interesting to note that the LSB galaxies overlap with our sample galaxies albeit with a larger scatter. The fit to our sample galaxies also appears to be a good fit for LSB galaxies. From the figure (see also Sec. 3.4) one can



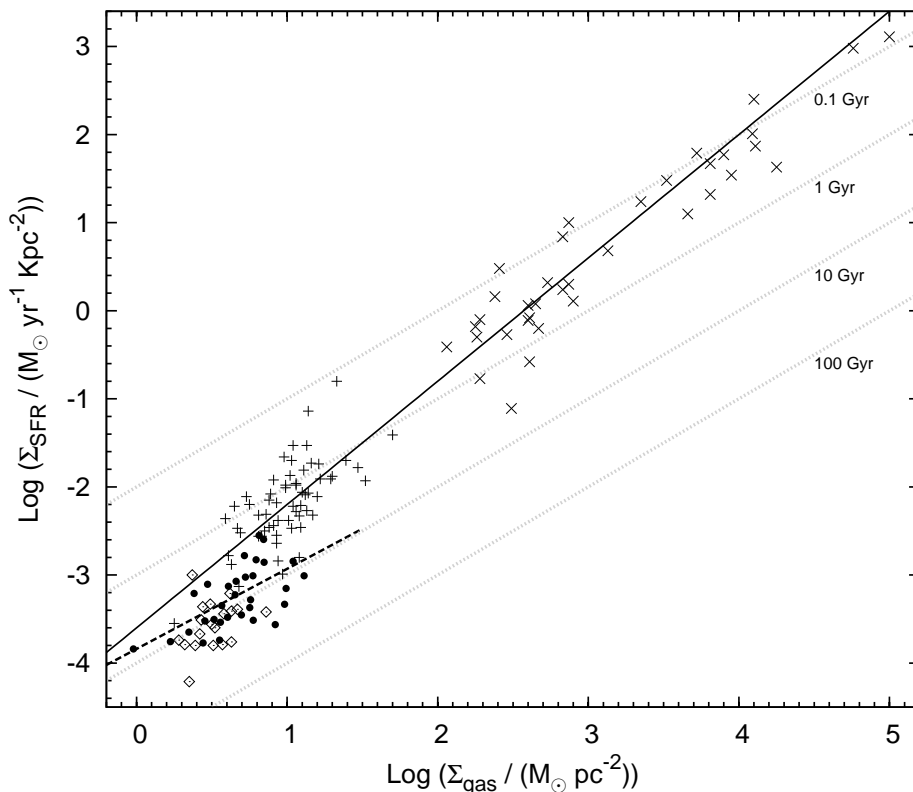


**Figure 8.** The ‘canonical’ disk-averaged Kennicutt-Schmidt law compared to our results. Crosses and pluses represent circumnuclear starbursts and spirals from Kennicutt (1998) respectively. Open diamonds represent LSB galaxies from Wyder et al. (2009). Our sample galaxies (SFR estimated using FUV emission) are represented by filled circles, without errorbars for clarity. The ‘canonical’ Kennicutt-Schmidt law is shown as the bold line. The best fit Schmidt law to our sample galaxies is shown as the dashed line. Faint grey dotted lines mark different gas consumption timescales.

see that our the gas consumption timescales for are sample galaxies is  $\sim 10$  Gyr. This is significantly smaller than the estimated timescales ( $\sim 100$  Gyr, Bigiel et al. 2010) for the outskirts of spiral galaxies. It is also significantly larger than the estimated gas consumption timescales ( $\sim 2$  Gyr) in the inner parts of spiral galaxies (see e.g. Leroy et al. 2013).

Ideally, one would like to look at the relation between the molecular gas and star formation, as opposed to the atomic gas and star formation. Unfortunately, it is not possible to do such a study for the faint dwarfs, since there is essentially no data on their molecular gas content. Determination of the molecular hydrogen fraction remains difficult for low metallicity galaxies like the ones in our present sample due to the very high (expected) CO-to-H<sub>2</sub> conversion factors (Bolatto, Wolfire & Leroy 2013). CO measurements for galaxies with metallicities comparable to the upper range of metallicities for our sample galaxies are only now being done (Elmegreen et al. 2013), though the Atacama Large Millimeter Array (ALMA) might change that soon. In general however, one would expect the molecular gas content of low mass dwarf irregular galaxies to be low. Models for star formation in such environments have been presented by Krumholz (2013). Ostriker, McKee & Leroy (2010) also present models for star formation in regions of low  $\Sigma_{\text{SFR}}$ . The model by Ostriker, McKee & Leroy (2010) assumes that the atomic gas has achieved two phase thermal equilibrium while in Krumholz (2013) model, the formation of the CNM phase of atomic gas as well as

the atomic to molecular transition and the star formation rate are set by the requirements of hydrostatic balance and not by two-phase equilibrium. Bolatto et al. (2011) have proposed a modification to the Ostriker, McKee & Leroy (2010) model which brings it into agreement with the data for the low metallicity conditions of the SMC. We compare these models with our data in Fig. 9. In the case of Krumholz (2013) model, we use the model with metallicity  $\sim 0.1$  times the solar metallicity, (which corresponds well to the estimated metallicity of our sample galaxies) with clumping factor  $f_c = 5$  since for our sample galaxies we average flux over  $\sim \text{kpc}$  size star-forming disks. The dashed and dotted lines are for  $\rho_{sd} = 0.01$ ,  $f_w = 0.5$ , and  $\rho_{sd} = 0.03$ ,  $f_w = 0.07$ .  $\rho_{sd}$  is the volume density of stars and dark matter, (in units of  $M_\odot \text{pc}^{-3}$ ) and the range used above corresponds well to the expected range for our sample galaxies.  $f_w$  is a measure of the distribution of atomic gas in the different phases, and Krumholz (2013) argues that the values used above bracket what one would expect in astrophysical situations. The solid grey line is the Bolatto et al. (2011) modification of the Ostriker, McKee & Leroy (2010) model with metallicity  $\sim 0.1$  times the solar metallicity and  $\rho_{sd} = 0.01$ . As can be seen, both models significantly under-predict the observed star formation rate for our sample galaxies. It is worth noting however that the points from Bigiel et al. (2010) lie within the region where stochastic effects would lead to significant uncertainty in the estimated star formation rate (see the discussion in Section. 3.1).

As mentioned above, the molecular gas content of our galaxies

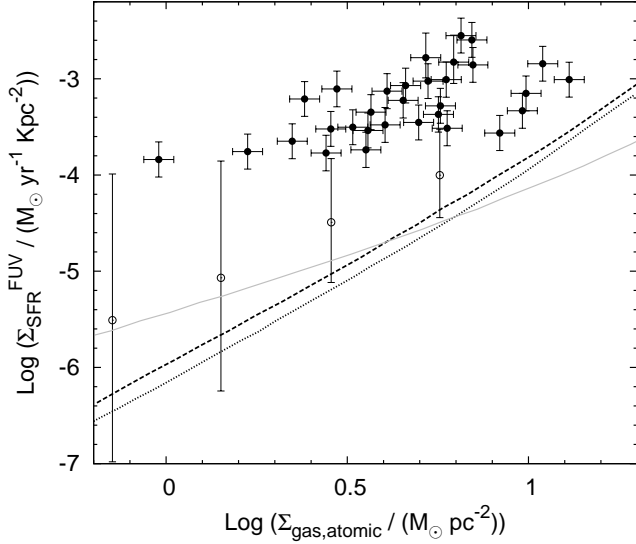


**Figure 9.** Data for the ‘trustworthy’ galaxies in our sample is shown as the filled circles. The hollow circles with error bars show the median and scatter of  $\sim 1$  kpc size regions in outskirts of spiral galaxies from Bigiel et al. (2010). The dashed and dotted lines show the expected variation of  $\Sigma_{\text{SFR}}$  with  $\Sigma_{\text{gas}}$  from Krumholz (2013) with the model parameters being  $f_c = 5$ ,  $\rho_{sd} = 0.01$ ,  $f_w = 0.5$  and  $f_c = 5$ ,  $\rho_{sd} = 0.03$ ,  $f_w = 0.07$  respectively. The grey line shows the expected variation of  $\Sigma_{\text{SFR}}$  with  $\Sigma_{\text{gas}}$  according to the modification of the Ostriker, McKee & Leroy (2010) model in Bolatto et al. (2011) with the model parameter  $\rho_{sd} = 0.01$ . All the three models plotted here are for 0.1 times the solar metallicity (see text for details).

is currently unknown. If we assume that the star formation rate is an indicator of the molecular gas content, then we can turn the question around, and try and estimate the molecular gas fraction in our sample galaxies from the observed  $\Sigma_{\text{SFR}}$ . In the outskirts of disk galaxies at least, this approach would be reasonable – Schrubba et al. (2011) show that even in the atomic gas dominated outskirts of the disk galaxies, the  $\Sigma_{\text{SFR}} - \Sigma_{\text{H}_2}$  relation is similar to that in the molecule rich regions. Two recent studies, viz. Leroy et al. (2013) and Momose et al. (2013) propose significantly different estimates of the relation between  $\Sigma_{\text{SFR}}$  and  $\Sigma_{\text{H}_2}$ . To explore the range of possibilities we use both of these estimates. From the relationship given by Leroy et al. (2013) we get a typical molecular fraction  $f_{\text{H}_2} \sim 0.05$  for our sample galaxies, while the somewhat steeper relation given in Momose et al. (2013) gives  $f_{\text{H}_2} \sim 0.4$ . A molecular fraction of  $\sim 0.4$  appears somewhat large for our sample galaxies considering the non-detection of CO emission even in the most luminous of our sample galaxies (see Taylor, Kobulnicky & Skillman 1998; Leroy et al. 2005; Buyle et al. 2006; Schrubba et al. 2012). However even the lower value estimated from the Leroy et al. (2013) relation is  $\sim 2$  times larger than that estimated for WLM, which has  $Z \sim 0.13$  Elmegreen et al. (2013).

### 3.4 Comparing total HI available to the total SFR

We restricted our study of SFR and gas surface densities to within the ‘star-forming disk’ of galaxies without any obvious signs of their HI disks being morphologically disturbed, for reasons described previously. But using this strategy meant we were discount-

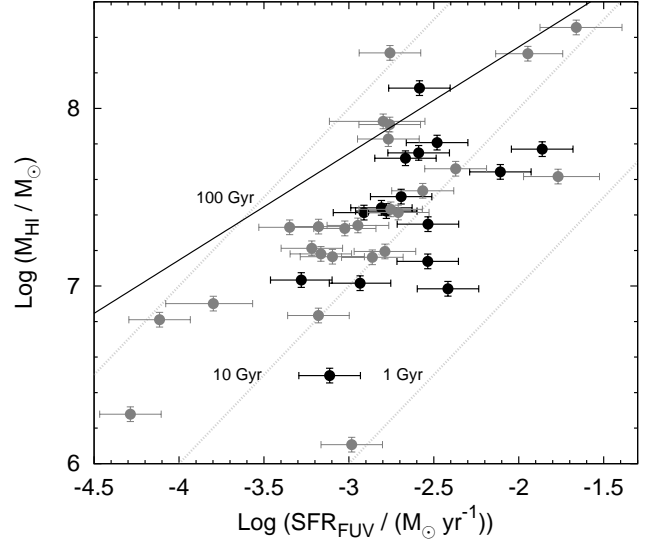


**Figure 10.** Total mass of HI plotted against to the total star formation rate of galaxies with (black points) and without (grey points) infrared data. The bold line is the best fit relation from Doyle & Drinkwater (2006) for HI flux selected galaxies more massive than our sample (see text for details). The dotted lines indicate the loci for different gas consumption timescales.

ing the (sometimes considerable) amount of HI present outside the ‘star-forming disk’ (see Figure A1) and its potential to be a fuel for star formation. We were also missing out on the relation between gas and star formation in the nine galaxies with morphologically disturbed HI. To address these issues, we do a comparison of the total star formation rate and the total HI mass of our sample galaxies in Figure 10. The total HI masses for all the galaxies except UGCA 438 are taken from Begum et al. (2008) which were calculated using the coarsest resolution (5 Kλ) HI data cubes. For UGCA 438 we calculated the total HI mass from the 400 pc resolution HI map used in this study. We use all the 41 galaxies in our sample with FUV data for we calculate the total SFRs using FUV, the more trustworthy tracer of star formation for low SFRs. Doyle & Drinkwater (2006) did a similar comparison for HI selected nearby galaxies from the HIPASS survey with HI masses somewhat larger than that of our sample galaxies (i.e. ranging from a few times  $10^8 M_\odot$  to a few times  $10^{10} M_\odot$ .) They found a power law relation between total SFR and HI mass with a slope of  $\sim 0.6$ , this is shown in Figure 10 as a solid line. Our sample galaxies tend to lie below this line. This means that while dwarf galaxies do convert their gas to stars somewhat less efficiently than spirals, the process is not as inefficient as the extrapolation of the Doyle & Drinkwater (2006) relationship would suggest. From the total HI mass and total SFR, the mean (median) gas consumption timescales for our sample galaxies is  $\sim 18(24)$  Gyr. While this is about a factor of  $\sim 2$  larger than the values estimated using the gas within the star forming disk, it is still significantly smaller than the estimated timescales ( $\sim 100$  Gyr, Bigiel et al. 2010) for the outer parts of disk galaxies.

## 4 SUMMARY

We compare the global average star formation rate density  $\Sigma_{\text{SFR}}$ , as measured using different tracers with the average atomic gas sur-

face density  $\Sigma_{\text{gas,atomic}}$  for a sample of dwarf galaxies drawn from the FIGGS survey. We use the H $\alpha$  FUV and 24  $\mu\text{m}$  fluxes to estimate  $\Sigma_{\text{SFR}}$ . The differences between the  $\Sigma_{\text{SFR}}$  computed with and without corrections for dust are small for most of the galaxies in our sample, consistent with their low metallicity. Excluding galaxies with  $\Sigma_{\text{SFR}}$  too low to be reliably measured, as well as galaxies with disturbed HI distributions, we find a nearly linear relation between  $\Sigma_{\text{SFR}}$  and  $\Sigma_{\text{gas}}$  with a gas consumption time scale of  $\sim 10$  Gyr. The typical gas consumption timescales of the star forming disks of dwarf galaxies is hence intermediate between that in the inner molecule rich and the outer molecule poor regions of spiral galaxies.

## ACKNOWLEDGMENTS

Some of the data presented in this paper were obtained from the Multimission Archive at the Space Telescope Science Institute (MAST). STScI is operated by the Association of Universities for Research in Astronomy, Inc., under NASA contract NAS5-26555. Support for MAST for non-HST data is provided by the NASA Office of Space Science via grant NAG5-7584 and by other grants and contracts. We thank the staff of the GMRT who have made the observations used in this paper possible. GMRT is run by the National Centre for Radio Astrophysics of the Tata Institute of Fundamental Research. SSK and IDK acknowledge that this work was supported by the Russian Foundation for Basic Research through grant 13-02-92690. We thank Ayesha Begum for providing the visibilities which were used to derive the HI maps used in this work. SR thanks Maryam Arabsalmani for helping with the Monte-Carlo simulations for fitting data with asymmetric errorbars. SR thanks Guinevere Kauffmann for helpful discussions regarding this work.

## REFERENCES

- Asplund M., Grevesse N., Jacques Sauval A., Scott P., 2009, *ARA&A*, 47, 481
- Begum A., Chengalur J. N., Karachentsev I. D., Sharina M. E., Kaisin S. S., 2008, *MNRAS*, 386, 1667
- Bigiel F., Leroy A., Walter F., Blitz L., Brinks E., de Blok W. J. G., Madore B., 2010, *AJ*, 140, 1194
- Bolatto A. D., Wolfire M., Leroy A. K., 2013, *ARA&A*, 51, 207
- Bolatto A. D. et al., 2011, *ApJ*, 741, 12
- Bouchard A., Da Costa G. S., Jerjen H., 2009, 137, 3038
- Buyle P., Michielsen D., De Rijcke S., Ott J., Dejonghe H., 2006, *MNRAS*, 373, 793
- Carraro G., Geisler D., Villanova S., Frinchaboy P. M., Majewski S. R., 2007, *A&A*, 476, 217
- Dale D. A. et al., 2009, *ApJ*, 703, 517
- da Silva R. L., Fumagalli M., Krumholz M. R., 2014, *arXiv:1403.4605*
- Doyle M. T., Drinkwater M. J., 2006, *MNRAS*, 372, 977
- Ekta B., Chengalur J. N., 2010, *MNRAS*, 406, 1238
- Elmegreen B. G., Rubio M., Hunter D. A., Verdugo C., Brinks E., Schruba A., 2013, *Nat.*, 495, 487
- Engelbracht C. W., Rieke G. H., Gordon K. D., Smith J.-D. T., Werner M. W., Moustakas J., Willmer C. N. A., Vanzì, L., 2008, 678, 804
- Fu J. et al., 2013, *MNRAS*, 434, 1531
- Genovali K., et al., 2014, *A&A*, 566, A37
- Governato F. et al., 2010, *Nature*, 463, 203
- Hao C.-N., Kennicutt Jr. R. C., Johnson B. D., Calzetti D., Dale D. A., Moustakas J., 2011, *ApJ*, 741, 124
- Hermanowicz M. T., Kennicutt R. C., Eldridge J. J., 2013, 432, 3097
- Hopkins P. F., Keres D., Onorbe J., Faucher-Giguere C.-A., Quataert E., Murray N., Bullock J. S., 2013, *arXiv:1311.2073*
- Hunter D. A., Elmegreen B. G., Ludka B. C., 2010, *AJ*, 139, 447
- Kaisin S. S., Karachentsev I. D., 2008, *A&A*, 479, 603
- Kaisin S. S., Karachentsev I. D., Kaisina E. I., 2011, *Ap*, 54, 315
- Karachentsev I. D., Kaisin S. S., 2007, *AJ*, 133, 1883
- Karachentsev I. D., Kaisin S. S., 2010, *AJ*, 140, 1241
- Karachentsev I. D., Kaisina E. I., 2013, *AJ*, 146, 46
- Karachentsev I. D. et al., *AJ*, 145, 101
- Kauffmann G., 2014, 441, 2717
- Kennicutt Jr. R. C., 1998, *ApJ*, 498, 541
- Kennicutt Jr. R. C., Evans II N. J., 2012, *ARA&A*, 50, 531
- Kennicutt Jr. R. C., Lee J. C., Funes J. G., Sakai S., Akiyama S., 2008, *ApJS*, 178, 247
- Kennicutt Jr. R. C. et al., 2009, *ApJ*, 703, 1672
- Krumholz M. R., 2013, *MNRAS*, 436, 2747
- Lee J. C. et al., 2009, *ApJ*, 706, 599
- Leitherer C. et al., 1999, *ApJSS*, 123, 40
- Leroy A., Bolatto A. D., Simon J. D., Blitz L., 2005, *ApJ*, 625, 763
- Leroy A. K. et al., 2012, *AJ*, 144, 3
- Leroy A. K. et al., 2013, *AJ*, 146, 19
- Mac Low M.-M., Ferrara A., 1999, *ApJ*, 513, 142
- Marble A. R. et al., 2010, *ApJ*, 715, 506
- McKee C. F., Ostriker E. C., 2007, *ARA&A*, 45, 565
- Meurer G. R. et al., 2006, *ApJSS*, 165, 307
- Meurer G. R. et al., 2009, *ApJ*, 695, 765
- Momose R. et al., 2013, *ApJ*, 772, L13
- Moustakas J., Kennicutt Jr. R. C., 2006, *ApJS*, 164, 81
- Ostriker E. C., McKee C. F., Leroy A. K., 2010, *ApJ*, 721, 975
- Pilyugin L. S., Thuan T. X., 2005, *ApJ*, 631, 231
- Raiter A., Schaerer D., Fosbury R. A. E., 2010, *A&A*, 523, 64
- Relaño M., Kennicutt Jr. R. C., Eldridge J. J., Lee J. C., Verley S., 2012, *MNRAS*, 423, 2933
- Roychowdhury S., Chengalur J. N., Begum A., Karachentsev I. D., 2009, *MNRAS*, 397, 1435
- Roychowdhury S., Chengalur J. N., Kaisin S. S., Begum A., Karachentsev I. D., 2011, *MNRAS*, 414, L55
- Roychowdhury S., Chengalur J. N., Karachentsev I. D., Kaisina E. I., 2013, *MNRAS*, 436, L104
- Schaye J., Dalla Vecchia C., 2008, *MNRAS*, 383, 1210
- Schruba A. et al., 2011, *AJ*, 142, 37
- Schruba A. et al., 2012, *AJ*, 143, 138
- Schmidt M., 1959, *ApJ*, 129, 243
- Silich S., Tenorio-Tagle G., 2001, *ApJ*, 552, 91
- Taylor C. L., Kobulnicky H. A., Skillman E. D., 1998, *AJ*, 116, 2746
- Weidner C., Kroupa P., 2005, *ApJ*, 625, 754
- Weisz D. R. et al., 2012, *ApJ*, 744, 44
- Wyder T. K. et al., 2009, *ApJ*, 696, 1834

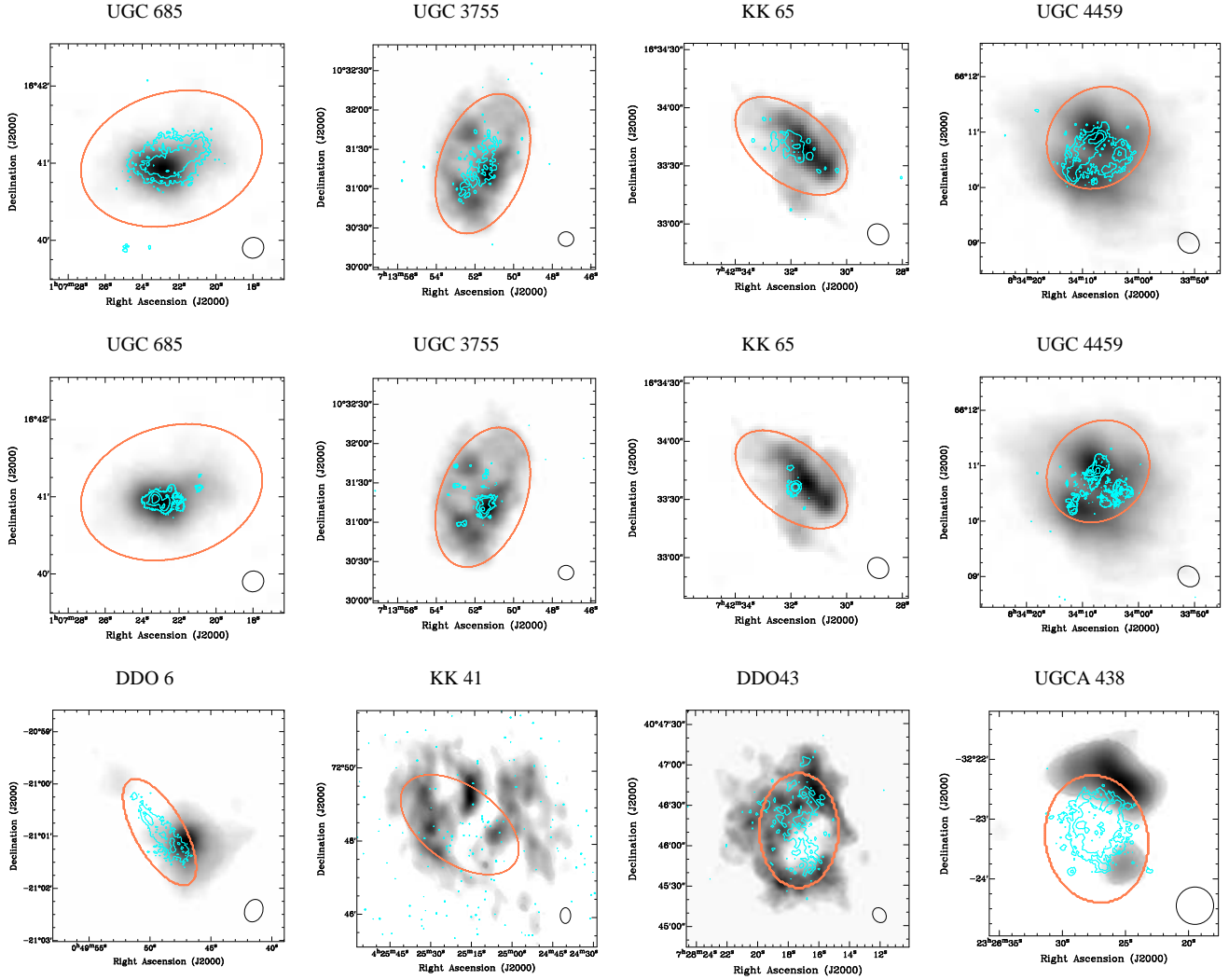


**Figure A1.** SFR indicator contours in cyan overlaid on HI column density in greyscale for representative sample galaxies (for the full set of overlays see the online version). The upper and middle rows show a set of galaxies with undisturbed HI morphology, with FUV emission in cyan for the upper row and  $H\alpha$  emission in cyan for the middle row. The lower row shows a set of galaxies with disturbed HI morphology with FUV emission in cyan. The Holmberg ellipse in each case is shown in orange. The level of the first contour is arbitrarily chosen so that traces of background emission are present, and subsequent contours are in multiples of 4. The HI beams are shown at the bottom right corner of each panel.

## APPENDIX A: VISUAL COMPARISON OF HI AND STAR FORMATION

This paper has been typeset from a  $\text{\LaTeX}$  file prepared by the author.